Engineering Fracture Mechanics 188 (2018) 361–380

Contents lists available at ScienceDirect

Engineering Fracture Mechanics

journal homepage: www.elsevier.com/locate/engfracmech

Continuous-discontinuous cellular automaton method for cohesive crack growth in rock

Fei Yan *, Xia-Ting Feng, Jia-He Lv, Peng-Zhi Pan, Shao-Jun Li

State Key Laboratory of Geomechanics and Geotechnical Engineering, Institute of Rock and Soil Mechanics, Chinese Academy of Sciences, Wuhan 430071, China

ARTICLE INFO

Article history:
Received 15 June 2017
Received in revised form 6 September 2017
Accepted 6 September 2017
Available online 12 September 2017

Keywords:
Continuous-discontinuous cellular automaton method
Cohesive cracks
Rock fractures
Discontinuous approximation
Alternative near-tip function

ABSTRACT

A group of nonsingular enrichment functions is proposed for an exact representation of the cohesive stresses, which are consistent with a nonsingular asymptotic stress field around a crack tip. An improvement in the adaptive crack tip polar coordinate is proposed for treating the local polar coordinate error. Finally, a discontinuous cellular automation model was developed, including a cell model, cell state, and updating rules. Combined with these developments and the cohesive rock model, a continuous-discontinuous cellular automaton method (CDCA) for a cohesive crack analysis is proposed, through which the calculation is only limited to the cell locality without re-meshing, and therefore, no assembled global stiffness matrix is required. Numerical simulations reveal the accuracy and efficiency of the presented method.

1. Introduction

With regard to a quasi-brittle material such as concrete or rock, a fracture process zone exists around the crack tip of the structure and includes fracturing to significant damage. Actually, the material is not fully cracked in this area, and it can still bear a certain amount of cohesion. Under the assumptions of the linear elastic fracture theory, stress at the crack tip becomes theoretically infinite; however, from a physical viewpoint, no material can withstand such an infinite amount of stress. Neither linear elastic fracture mechanics nor nonlinear fracture mechanics can be used to predict the crack propagation in concrete or rock structures. Therefore, a numerical simulation on cohesive crack propagation is very important for rock and concrete engineering.

The cohesive crack model is generally accepted as a realistic simplification of the fracture of brittle materials, and was first proposed by Barenblatt [1] and Dugdale [2]. Barenblatt applied the model to analyze the brittle fracture behavior, and Dugdale introduced it to model the ductile fracture behavior. The model was then experimentally proven reliable for rock-like and quasi-brittle materials [3]. Shortly thereafter, Ngo and Scordelis [4] and Hillerborg, Modeer, and Petersson [5] applied the cohesive crack model to simulate the softening damage of concrete structures, and Elices et al. [6] discussed its advantages and limitations.

In recent years, a number of numerical methods have been proposed to solve the cohesive crack propagation problem. Clearly, when potential crack paths are limited to inter-element boundaries, the crack paths are highly dependent on the meshing structure. Although a finite element method (FEM) is not the best numerical method for solving such problems,

* Corresponding author at: State Key Laboratory of Geomechanics and Geotechnical Engineering, Institute of Rock and Soil Mechanics, Chinese Academy of Sciences, Xiaohongshan, Wu Chang, Wuhan 430071, China.
E-mail address: fyan@whrsm.ac.cn (F. Yan).

http://dx.doi.org/10.1016/j.engfracmech.2017.09.007
0013-7944/

Nomenclature

$\mathbf{a}$	vector of additional degree of nodal freedom for strong discontinuity
$\mathbf{b}_f$	body force vector
$\mathbf{b}_i^l$	vector of additional degrees of nodal freedom for crack tip field
$\mathbf{B}_i^\alpha$	derivative matrix of shape function matrix
c_c	cohesion angle
c_s	crack surface state
$\mathbf{d}$	regular displacement vector
$\mathbf{D}$	elasto-plastic constitutive matrix
E	Young's modulus
$\mathbf{f}^{coh}$	cohesive force
$\mathbf{f}_i^\alpha$, $\mathbf{f}_i^l$	nodal force for normal and frictional freedom
f_n	loading or unloading factor
F_l	crack tip enrichment function
F_{a_i}	unbalanced nodal force
$H(\xi)$	heaviside function
$\mathbf{k}_i^u$, $\mathbf{k}_i^{a,b}$, $\mathbf{k}_i^c$	stiffness related to the traditional nodal freedom, additional nodal freedom, and cohesive
k_n, k_s	normal and shear stiffness constants
$\mathbf{K}_\mathrm{i}$	nodal stiffness
n, m	node number of an element
$\mathbf{n}(\mathbf{x})$	unit outward normal vector for point $\mathbf{x}$
$\mathbf{n}(\mathbf{x},t)$	positive direction of crack on point $\mathbf{x}$
$N_j(\mathbf{x})$	classical finite element shape function
$\tilde{\mathbf{N}}$	shape function matrix related to the relative displacement
$\hat{\mathbf{N}}$	shape function related to cohesive displacement field
$\mathbf{p_N}$, $\mathbf{p_T}$	normal and tangential pressures
r	polar coordinates, polar distance
$\mathbf{r}$	residual
$\mathbf{t}(\mathbf{x})$	tangential vector for point $\mathbf{x}$
$\mathbf{t}^{coh}$	cohesive stress
t_n^{coh}, t_t^{coh}	cohesive stress component in normal and tangential directions
$\hat{\mathbf{t}}$	given traction boundary condition
$\mathbf{u}(\mathbf{x})$	displacement vector on point $\mathbf{x}$
$\mathbf{u}$, $\hat{\mathbf{u}}$	displacement vector and given displacement boundary condition
$\mathbf{u}^{s+}$, $\mathbf{u}^{s-}$	displacement vector on crack surface S^+ and S^-
$\tilde{\mathbf{u}}$	relative displacement vector between crack surfaces
w_n, $w_n^{\max}$, w_n^c	normal separation at crack surface, history value, critical value
w_t, w_t^c	tangential separation at crack surface and critical value
$\mathbf{w}_c(\mathbf{x})$	relative displacement between crack surfaces
$\mathbf{w}$, $\mathbf{t}$	displacement and traction vectors
θ	polar coordinate, polar angle
μ_c	Coulomb friction coefficient
v	Poisson ratio
$\boldsymbol{\sigma}$	stress vector
$\phi_j^i(\mathbf{x},t)$	distance function to crack front of crack j
φ_c	Friction angle
$\varphi_j(\mathbf{x},t)$	distance function to crack surface of crack j
$\Delta\mathbf{u}_i$, $\Delta\mathbf{f}_i$	increment of nodal displacement and nodal force

owing to its domain re-meshing during crack propagation and its fine meshing for representing a high gradient stress at a crack tip, some studies associating cohesive crack growth problems with FEM have been presented [7,8]. Recently, polygon-based finite elements [9], the Voronoi cell FEM [10], and a generalized variable FEM [11,12] have been implemented to model the cohesive crack propagation. To avoid the difficulties involved in fully automatic cohesive crack propagation modeling, a scale boundary finite element method and a coupled finite element and scale boundary element method have both been developed [13,14].

As a widely used numerical method, the boundary element method (BEM) has also been used by many researchers over the past decades for cohesive crack growth modeling [15–18], and a dual reciprocity BEM and an alternative nonlinear BEM

formulation have been used. Furthermore, a symmetric Galerkin boundary element method has been proposed for dealing with quasi-brittle fracture and frictional contact problems [19], and a symmetric Galerkin multi-zone boundary element method has been developed for the growth of multiple cohesive cracks [20].

Owing to their much greater smoothness, flexibility, and a lack of meshing, mesh-free methods are a good alternative for crack propagation problems compared to the FEM and BEM. Modeling of the crack propagation using the mesh-free Element-free Galerkin method (EFGM) was first conducted by Belytschko et al. [21], and furthermore, Rabczuk and Zi [22] proposed a mesh-free method based on the local partition of unity for cohesive cracks, geometrically combined nonlinear theory and an extended EFG to solve three-dimensional cohesive crack fracturing for reinforced concrete structures [23]. In addition, Goudarzi et al. [24] developed an enriched EFGM for analyzing cohesive cracking in a saturated porous medium. Moreover, Jaskowiec and Cichon [25] coupled FEM and EFGM with a dynamic decomposition for a 2D quasi-brittle crack growth analysis.

In recent years, the extended finite element method (XFEM) has been widely used for crack propagation analyses because it can completely avoid re-meshing for crack dynamic fracturing. Wells and Sluys [26] and Moes et al. [27] first applied XFEM to model the growth of arbitrary cohesive cracks. In addition, Zi and Belytschko [28] proposed a new crack-tip element for modeling static cohesive cracks, in which all cracked elements are enriched by the sign function such that no blending of the local partition of unity is required. Similarly, Mariani and Perego [29] and Mergheim et al. [30] proposed the use of computational modeling and a methodology for the simulation of quasi-static cohesive crack propagation in quasi-brittle materials. In addition, some other applications of cohesive crack propagation for elastostatics and elastodynamics using XFEM [31–34] have recently been reported.

Differing from the node-level enrichment of XFEM, embedded crack models (ECMs) [35,36], which are based on an element level of enrichment, have also been widely used for cohesive crack propagation because this approach can also model cohesive crack propagation without re-meshing; however, its shortcoming is that the displacement approximation is non-conforming, and the resulting stiffness matrix is unsymmetrical.

Almost all of the above methods require an assembled global stiffness matrix in their computations, which is time-consuming and requires high memory consumption, because different nodes have different numbers of node freedoms. However, the cellular automation (CA) theory can be used to overcome this defect, through which no assembled global stiffness matrix is required. The CA theory was initially derived from the self-organization theory in biology. The theories and applications of CA to solid mechanics have developed rapidly over the past decades, including those by Eugenio and Rasetti [37], who developed a CA model for elasticity, and Olami et al. [38], who used CA in earthquake modeling. In addition, Abdellaoui et al. [39] applied CA for the contact problem, and Canyurt et al. [40] developed a CA model for structural analysis and optimization. Moreover, Shen et al. [41] developed elastic updating rules and applied them for solving the solid mechanical problem. Gurdal and Tatting [42] built a lattice model to solve the plane lattice deformation problem, and Leamy and Hopman [43,44] developed an application of cellular automaton modeling for use with the elastodynamics problem and arbitrary two-dimensional geometries. Further, Feng et al. [45] used the lattice CA model to simulate the failure process of heterogeneous rocks. Based on the lattice CA model, Yan et al. [46,47] proposed a continuous-discontinuous cellular automaton method for tensile propagation of multiple cracks, and furthermore, they [48,49] developed a traditional frictional contact method for the compression shear propagation of multiple cracks.

For elastic and plastic solids, Popov and Psakhie [50] proposed a movable CA for the modeling of elastoplastics, Xiao [51] employed CA to simulate elastic wave propagation, and Kwon and Hosiglu [52] applied a coupling of the lattice Boltzmann method, finite element method, and cellular automata to an analysis of wave propagation problems. Khvastunkov and Leggoe [53] combined the finite element method with CA and studied random spatial heterogeneity distributions.

Based on the traditional frictional contact method used in a continuous-discontinuous cellular automaton [48,49], a cohesion model for rock cracks was developed, and a novel continuous-discontinuous cellular automaton (CDCA) method for cohesive crack propagation modeling has been implemented in detail. In a cohesive crack model, there are no singularities at the crack tip, and therefore, a crack tip enrichment with singular functions is not suitable; thus, a group of new nonsingular additional enrichment functions is employed instead of the traditional singular enrichment functions, which are consistent with a nonsingular asymptotic stress field around a cohesive crack tip. Aiming at determining a devious crack path, an improvement in an adaptive crack tip polar coordinate is proposed for treating the local polar coordinate error caused by a devious crack-fracturing segment. Based on a cohesive crack model of quasi-brittle materials, a cellular automation model for cohesive cracks has been developed, including a cell model, cell state, and updating rules. Combined with the above theories, the CDCA for a cohesive crack propagating analysis is proposed, in which the cracking path can pass through any element and no re-meshing is required. In addition, the calculation is only limited to the cell locality, and no assembled global stiffness matrix is needed, which can help avoid some of difficulties caused by the different nodal freedoms for different nodes. Finally, the effectiveness of the proposed approach is demonstrated through simulations of cohesive crack growth in rock.

2. Cohesive model and variational formulation

Consider a body Ω with crack S, as shown in Fig. 1. The crack tip includes a physical tip and fictitious tip, and crack S includes two separate surfaces S^+ and S^-. According to the cohesive crack theory, the relation between crack open displacement (COD) and cohesive stress, and the local model of a cohesive crack tip, can be given as shown in Fig. 2.

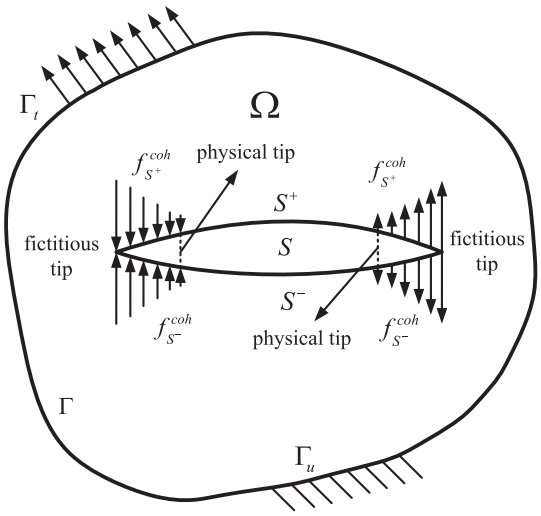

Fig. 1. Model of cohesive crack problem.

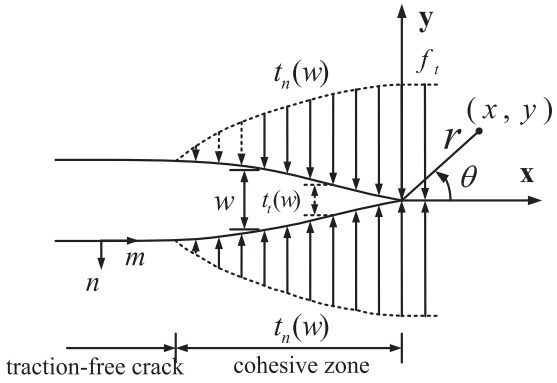

Fig. 2. Local model of crack tip.

2.1. Cohesive model

For quasi-brittle materials, the fracture process zone around a crack tip is large enough to cause nonlinear effects, which cannot be neglected. To consider these effects, cohesive crack models were first proposed by Barenblatt [1] and Dugdale [2], which were further developed and applied [3–5,54,55]. A number of non-uniform traction models have been proposed in the past years, and using these cohesive zone models, the tractions around the crack decrease and vanish with an increasing separation of the crack surfaces. These models share the same concept as softening behavior, where the traction has the maximum intensity at the point of a fictitious tip and the minimum value at the point of a physical tip, as shown in Fig. 2.

Non-uniform models in terms of traction-opening curves include uniform, linear, bilinear, and exponential models, and in the present paper, a three-parameter rate-independent linear cohesive model is employed, which was first proposed in [9,15,56], and the traction-separation behavior under loading and unloading cases can be seen in Fig. 3.

According to the cohesive crack model [26], a loading function can be defined as

$$f_n = w_n - w_n^{\max} \tag{1}$$

where w_n is the normal separation at the crack surface, a positive displacement indicates that the crack is opening, and $w_n^{\max}$ is the historic value of w_n, which is equal to the largest value of w_n in its cracking history. When a crack is opening, $f_n \geqslant 0$ indicates that the discontinuity is loading, and $f_n < 0$ indicates that it is unloading. The model assumes a free cohesive energy potential ϕ [26], and the traction across the cohesive surface is expressed as

$$\mathbf{t}^{coh} = t_n^{coh}\mathbf{n}(\mathbf{x}) + t_t^{coh}\mathbf{t}(\mathbf{x}) = \frac{\partial \phi}{\partial w_n}\mathbf{n}(\mathbf{x}) + \frac{\partial \phi}{\partial w_t}\mathbf{t}(\mathbf{x}) \tag{2}$$

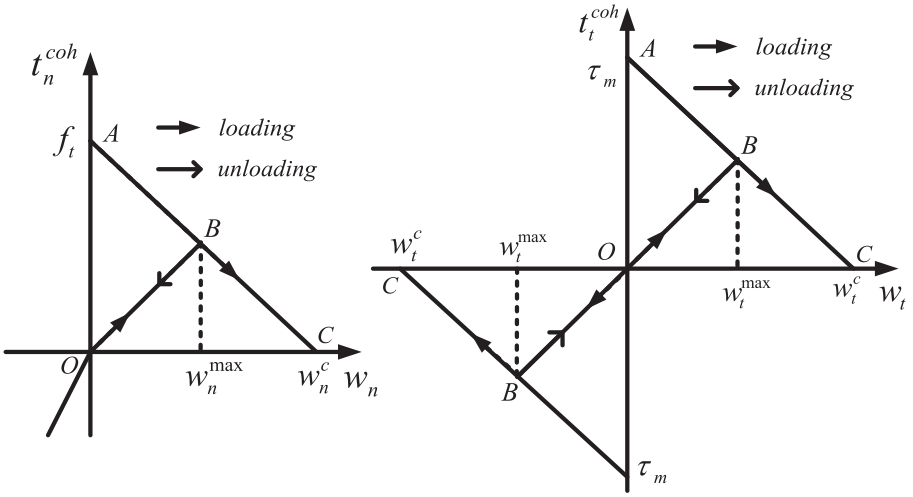

Fig. 3. Traction-separation behavior for linear cohesive crack model.

in which $\mathbf{n}(\mathbf{x})$ denotes the unit outward normal vector for point $\mathbf{x}$, and $\mathbf{t}(\mathbf{x})$ is the tangential vector for point $\mathbf{x}$; in addition, $\mathbf{t}^{coh}$ is the cohesive stress vector, and t_n^{coh} and t_t^{coh} are the cohesive stress components in the normal and tangential directions, respectively.

In this case, the normal cohesions of the crack surface can be given as follows:

$$\begin{aligned} t_n^{coh}(w_n) &= f_t\left(1-\tfrac{w_n}{w_n^c}\right) \quad \text{if } 0 \leqslant w_n \leqslant w_n^c \\ t_n^{coh}(w_n) &= 0 \qquad\qquad \text{if } w_n > w_n^c \end{aligned} \tag{3}$$

where w_n^c is the critical value of the crack opening displacement.

Similarly, one can obtain the following tangential traction:

$$\begin{aligned} t_t^{coh}(w_t) &= \tau_m\left(-1-\tfrac{w_t}{w_t^c}\right) \quad \text{if } -w_t^c \leqslant w_t \leqslant 0 \\ t_t^{coh}(w_t) &= \tau_m\left(1-\tfrac{w_t}{w_t^c}\right) \quad \text{if } 0 \leqslant w_t \leqslant w_t^c \\ t_t^{coh}(w_t) &= 0 \qquad\qquad \text{if } w_t > w_t^c \end{aligned} \tag{4}$$

In the present method, the effect between normal traction and tangential traction can be neglected, and thus, we can obtain the constitutive law of the present cohesive model, and traction $\mathbf{t}$ on a cohesive crack surface is thus related to the crack opening displacement $\mathbf{w}_c = [w_n, w_t]^T$ [14], which can be written as

$$\mathbf{t} = \begin{pmatrix} t_n^{coh} \\ t_t^{coh} \end{pmatrix} = \begin{bmatrix} \frac{\partial t_n^{coh}}{\partial w_n} & 0 \\ 0 & \frac{\partial t_t^{coh}}{\partial w_t} \end{bmatrix} \begin{Bmatrix} w_n \\ w_t \end{Bmatrix} = \begin{bmatrix} k_n & 0 \\ 0 & k_s \end{bmatrix} \begin{Bmatrix} w_n \\ w_t \end{Bmatrix} \tag{5}$$

where k_n and k_s are the secant stiffness determined by the normal and tangential softening laws shown in Fig. 3.

2.2. Variational formulation

Consider a body including a cohesive crack with tractions $\mathbf{f}^{coh}$ along the fracture process zone Γ_c. According to cohesive crack theory, the governing equations can be written as

$$\begin{aligned} &\text{div}(\boldsymbol{\sigma}) + \mathbf{b}_f = 0 \quad \text{in } \Omega \\ &\mathbf{n}(\mathbf{x}) \cdot \boldsymbol{\sigma} = \hat{\mathbf{t}} \quad \text{on } \Gamma_t \\ &\mathbf{u} = \hat{\mathbf{u}} \quad \text{on } \Gamma_u \\ &\mathbf{n}(\mathbf{x}) \cdot \boldsymbol{\sigma} = \mathbf{t}^{coh} \quad \text{on } \Gamma_s \end{aligned} \tag{6}$$

where $\boldsymbol{\sigma}$ is the stress tensor, $\mathbf{u}$ is the displacement vector, $\mathbf{b}_f$ is the body force, $\hat{\mathbf{t}}$ is the traction vector acting on an external surface Γ_t, and $\hat{\mathbf{u}}$ is the given displacement boundary condition on Γ_u.

Now, we assume that $\mathbf{t}^{coh}$ is simply related to the crack opening displacement $\mathbf{w}_c$. Then, the weak form of the equilibrium equation can be written [26,27,46–49] as follows:

$$W^{\text{int}} = W^{ext} + W^{coh} = \int_{\Omega} \boldsymbol{\sigma} \cdot \delta\boldsymbol{\varepsilon} d\Omega = \int_{\Omega} \mathbf{b}_f \delta\mathbf{u} d\Omega + \int_{\Gamma_t} \hat{\mathbf{t}} \delta\mathbf{u} d\Gamma - \int_{\Gamma_c} \mathbf{t}^{coh} (\delta\mathbf{u}^{s+} - \delta\mathbf{u}^{s-}) d\Gamma \tag{7}$$

in which $\boldsymbol{\varepsilon}$ is the strain tensor, $\mathbf{u}^{s+}$ is the displacement vector on crack surface S^+, and $\mathbf{u}^{s-}$ is the displacement vector on crack surface S^-.

3. Discontinuous cellular automaton for cohesive crack

3.1. Discontinuous enrichment for cohesive model

Compared to the infinite crack tip stress of a linear elastic fracture model, the crack tip stress of the cohesive crack model is finite, and the traditional infinite enriched function of a crack tip is therefore not suitable for the cohesive crack model. Although an analytical solution for the response near an arbitrary cohesive zone does not exist, the case of a cohesive zone associated with a straight crack within an isotropic linear domain was recently addressed. According to [57], the asymptotic displacement field of a cohesive crack tip for pure mode I can be given as follows:

$$u = \sum_{n=1} \frac{r^{\frac{(2n+1)}{2}}}{2\mu} a_{1n} \left[\left(\kappa + \frac{2n-1}{2} \right) \cos\frac{2n+1}{2}\theta - \frac{2n+1}{2} \cos\frac{2n-3}{2}\theta \right] \tag{8}$$

$$v = \sum_{n=1} \frac{r^{\frac{(2n+1)}{2}}}{2\mu} a_{1n} \left[\left(\kappa - \frac{2n-1}{2} \right) \sin\frac{2n+1}{2}\theta + \frac{2n+1}{2} \sin\frac{2n-3}{2}\theta \right] \tag{9}$$

where r and θ are respectively the radius and angle of the calculating point in a local crack tip coordinate system, Kolosov constant $\kappa = \frac{(3-\nu)}{(1+\nu)}$ for the plane stress problem, and $\kappa = 3 - 4\nu$ for the plane strain problem; in addition, a_{1n} is a coefficient, n is a variable from 1 to $+\infty$, $\mu = E/[2(1+\nu)]$ is the shear modulus, E is the elastic modulus, and ν is the Poisson ratio.

Furthermore, the asymptotic displacement field of a cohesive crack tip for pure mode II can be given as follows:

$$u = \sum_{n=1} \frac{r^{\frac{(2n+1)}{2}}}{2\mu} a_{2n} \left[\left(\kappa - \frac{2n-1}{2} \right) \sin\frac{2n+1}{2}\theta - \frac{2n+1}{2} \sin\frac{2n-3}{2}\theta \right] \tag{10}$$

$$v = -\sum_{n=1} \frac{r^{\frac{(2n+1)}{2}}}{2\mu} a_{2n} \left[\left(\kappa + \frac{2n-1}{2} \right) \cos\frac{2n+1}{2}\theta + \frac{2n+1}{2} \cos\frac{2n-3}{2}\theta \right] \tag{11}$$

According to Eqs. (8) and (9), the following special purpose functions for the crack tip enrichment are applied:

$$\{F_{l,l=1-4}\} = \left\{ r^{\frac{3}{2}} \sin\left(\frac{\theta}{2}\right), r^{\frac{3}{2}} \cos\left(\frac{\theta}{2}\right), r^{\frac{3}{2}} \sin(\theta) \sin\left(\frac{\theta}{2}\right), r^{\frac{3}{2}} \sin(\theta) \cos\left(\frac{\theta}{2}\right) \right\} \tag{12}$$

As is well known, the asymptotic displacement field of a cohesive crack tip in mixed mode can also include the functions of Eqs. (8)–(11), which can be given as the functions of the four parts in Eq. (12), which can in turn be used for a mixed-mode cohesive fracture.

3.2. Continuous-discontinuous cellular automaton discretization

According to the crack tip enrichment described in the previous section, we can obtain the shape function for a cohesive crack problem, which can be given as

$$\mathbf{u}(\mathbf{x}) = \sum_{j=1}^{n} N_j(\mathbf{x}) \mathbf{d}_j + \underbrace{\sum_{k=1}^{m} N_k(\mathbf{x}) (H(\varphi(\mathbf{x}, t)) - H(\varphi(\mathbf{x}_k, t))) \mathbf{a}_k}_{k \in P} + \underbrace{\sum_{i=1}^{t} N_i(\mathbf{x}) \left(\sum_{l=1}^{nf} (F_l(\mathbf{x}) - F_l(\mathbf{x}_i)) \mathbf{b}_i^l \right)}_{i \in T} = \tilde{\mathbf{N}} \{ \mathbf{d}\ \mathbf{a}\ \mathbf{b} \} \tag{13}$$

where $N_j(\mathbf{x})$ is the classical finite element shape function; $\mathbf{d}_j$ is the standard degree of freedom; $\mathbf{a}_k$ is a vector of the additional degree of nodal freedom for modeling a strong discontinuity; $\varphi(\mathbf{x}, t)$ and $\varphi(\mathbf{x}_k, t)$ are the distance from points $\mathbf{x}$ and $\mathbf{x}_k$ to the crack, respectively; n, m and t are node numbers of an element; nf is the number of basis functions for the enrichment function in Eq. (12); P represents the node sets penetrated by a crack; T denotes the crack tip nodes; $\mathbf{b}_i^l$ is a vector of additional degrees of nodal freedom for modeling the crack tip stress field [47–49]; $H(\xi)$ is the Heaviside function; and $\tilde{\mathbf{N}}$ is a shape function matrix of a discontinuous element. In addition, for a continuous element, the shape function is the same as the traditional finite element, which is

$$\mathbf{u}(\mathbf{x}) = \sum_{j=1}^{n} N_j(\mathbf{x}) \mathbf{d}_j = \mathbf{N}\mathbf{d} \tag{14}$$

According to Eq. (13), we can obtain $H(\varphi(\mathbf{x},t))=1$ on a discontinuous surface of S^+, and $H(\varphi(\mathbf{x},t))=-1$ on a discontinuous surface of S^-. We can then obtain

$$\mathbf{w}_c(\mathbf{x})=\mathbf{u}_{S^+}-\mathbf{u}_{S^-}=2\underbrace{\sum_{k=1}^{m}N_k(\mathbf{x})\mathbf{a}_k}_{k\in P}+2\underbrace{\sum_{i=1}^{t}N_i(\mathbf{x})r\mathbf{b}_i^0}_{i\in T}=\hat{\mathbf{N}}\{\mathbf{ab}\} \tag{15}$$

where $\hat{\mathbf{N}}$ is the shape function related to a cohesive displacement field, and $\mathbf{b}_i^0$ is the first component of the vector of additional degrees of nodal freedom $\mathbf{b}_i$ for modeling the crack tip stress field.

Substituting Eqs. (13)–(15) into Eq. (7), we can obtain the following residual equation [47–49]:

$$\mathbf{r}(\mathbf{D})=\begin{Bmatrix}\mathbf{F}_{\text{ext}}^{u}-\mathbf{F}_{\text{int}}^{u}\\ \mathbf{F}_{\text{ext}}^{ab}-\mathbf{F}_{\text{int}}^{ab}-\mathbf{F}_{\text{int}}^{coh}\end{Bmatrix} \tag{16}$$

where $\mathbf{D}=\{\mathbf{dab}\}^T$, $\mathbf{F}_{\text{int}}^{u}(\mathbf{d},\mathbf{a})=\int_\Omega\mathbf{B}^{\mathbf{T}}\boldsymbol{\sigma}(\mathbf{d},\mathbf{a})d\Omega$, $\mathbf{F}_{\text{ext}}^{u}=\int_\Omega\mathbf{N}^{\mathbf{T}}\mathbf{b}_f d\Omega+\int_\Gamma\mathbf{N}^{\mathbf{T}}\hat{\mathbf{t}}d\Gamma$, $\mathbf{F}_{\text{int}}^{ab}(\mathbf{d},\mathbf{a},\mathbf{b})=\int_{\Omega^h\setminus S}\tilde{\mathbf{B}}^{\mathbf{T}}\boldsymbol{\sigma}(\mathbf{d},\mathbf{a})d\Omega$, and $\mathbf{F}_{\text{ext}}^{\text{ab}}=\int_{\Omega^h}\tilde{\mathbf{N}}^{\mathbf{T}}\mathbf{b}_f d\Omega+\int_{\Gamma^h}\tilde{\mathbf{N}}^{\mathbf{T}}\hat{\mathbf{t}}d\Gamma$, in which $\mathbf{B}$ is a derivative of a traditional finite element shape function matrix $\mathbf{N}$, and $\tilde{\mathbf{B}}$ is a derivative of the shape function matrix $\tilde{\mathbf{N}}$. In addition, the nodal force related to $\mathbf{f}^{coh}$ can be given as

$$\mathbf{F}_{\text{int}}^{coh}=\int_S\hat{\mathbf{N}}^T\mathbf{t}^{coh}dS \tag{17}$$

To solve this nonlinear problem, we iterate using Newton's method and cellular automaton updating rules, which are the same as in [47–49].

According to the cohesive model theory, the cell cohesive state c_s can be any one of four states, i.e., no fracturing, cohesive, fracturing and opening, or fracturing and closed, and c_s can be given as follows.

$$c_s=\begin{cases}=0 & \text{no fracturing}\\ =1 & \text{cohesive}\\ =2 & \text{fracturing and opening}\\ =3 & \text{fracturing and closed}\end{cases} \tag{18}$$

Based on the CA model, the calculation is located in any one cell for each update, and we can then obtain

$$\mathbf{K}_{\text{i}}=-\mathbf{r}'(\mathbf{D}) \tag{19}$$

where $\mathbf{K}_{\text{i}}$ can be divided into three groups, i.e., a $\mathbf{k}_i^u$ matrix related to the traditional nodal freedom, a $\mathbf{k}_i^{a,b}$ matrix related to the additional nodal freedom $\mathbf{a}$ or $\mathbf{b}$, and a $\mathbf{k}_i^c$ matrix related to the cohesive crack model, which can be given as

$$\mathbf{k}_i^u=\int_{\Omega_e}\mathbf{B}_i^T\mathbf{D}\mathbf{B}_i d\Omega \tag{20}$$

$$\mathbf{k}_i^{a,b}=\int_{\Omega_e}(\mathbf{B}_i^r)^T\mathbf{D}(\mathbf{B}_i^r)d\Omega\quad r=\mathbf{a},\mathbf{b} \tag{21}$$

$$\mathbf{k}_i^c=\int_{\Omega_e}\hat{\mathbf{N}}_i^T\mathbf{E}\hat{\mathbf{N}}_i d\Omega \tag{22}$$

where $\mathbf{B}_i$ is the matrix of the shape function derivatives of the traditional FEM method, and $\mathbf{B}_i^r$ is the matrix of the shape function derivatives of the enrichment function; for example, $r=\mathbf{a}$ represents the derivatives of the Heaviside function, $r=\mathbf{b}$ represents the derivatives of the crack tip enrichments, $\mathbf{D}$ is a constitutive matrix, and $\mathbf{E}$ is a constitutive matrix for the cohesive model, which can be given as

$$\mathbf{E}=\mathbf{T}^T\begin{bmatrix}k_n & 0\\ 0 & k_s\end{bmatrix}\mathbf{T} \tag{23}$$

where $\mathbf{T}$ is the transformation matrix from the global coordinate system to the local crack coordinate of the crack tip.

Actually, some subdomains are obtained according to the element type for a nodal matrix integration, which can be seen in Fig. 4. It can be seen in Eq. (12) that no singular integral is accounted for, and we can then obtain the following integration scheme:

$$\mathbf{k}_i^u=\int_{A1}\mathbf{B}_i^T\mathbf{D}\mathbf{B}_i d\Omega+\int_{A2}\mathbf{B}_i^T\mathbf{D}\mathbf{B}_i d\Omega+\int_{A3}\mathbf{B}_i^T\mathbf{D}\mathbf{B}_i d\Omega+\int_{A4}\mathbf{B}_i^T\mathbf{D}\mathbf{B}_i d\Omega \tag{24}$$

In addition, the same equations for a nodal force matrix and a cohesive stiffness matrix can be obtained according to Eq. (24).

According to the different states of a crack surface, the nodal matrix can be given as follows.

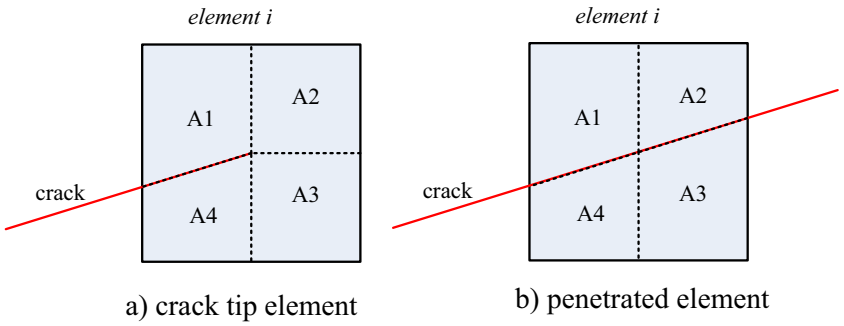

Fig. 4. Integration scheme of crack tip element and penetrated element.

$$\mathbf{K}_i = \begin{cases} \mathbf{k}_i^u & c_s = 0 \\ \mathbf{k}_i^u + \mathbf{k}_i^{a,b} + \mathbf{k}_i^c & c_s = 1 \\ \mathbf{k}_i^u + \mathbf{k}_i^{a,b} & c_s = 2 \\ \mathbf{k}_i^u + \mathbf{k}_i^{a,b} & c_s = 3 \end{cases} \tag{25}$$

3.3. Discontinuous cellular automaton for cohesive model

Through the continuous-discontinuous cellular model, the equilibrium state of the cell can be obtained through a one-another transfer of the information between nodes. The behavior of the cell is thought to be essentially local; in other words, the state of one cell is simply determined by the states of itself and its neighbors. There are three advantages to this theory. First, there is no need to assemble the global stiffness matrix, particularly for the enriched nodes, and the different degrees may bring about certain difficulties in the assembly operation, which can also save a great deal of computational memory. Second, it is easy to consider the local properties of the cell. Third, a large-scale simulation can be easily conducted owing to the easy implementation of a parallel algorithm.

The CDCA model is composed of a cell, cell space, cell state, crack, neighborhood, updating rules, and other elements, and the relationships among these components can be seen in [45,47–49].

3.3.1. Cell and its state

According to CDCA, a cell includes a common finite element cell, opening crack cell, cohesive crack cell, and common finite element cell, and the opening crack cell can be seen in [45,47–49]. Based on the cohesive crack model and CDCA theories, Fig. 5 shows that a series of physical and mechanical variations must be defined to determine the different states of a cohesive cell. A cohesive crack cell model is composed of the degree value vector of nodal freedom $\mathbf{u}^h = \{\mathbf{u}, \mathbf{a}, \mathbf{b}\}$, in which $\mathbf{u}$ is the traditional degree of nodal freedom, $\mathbf{a}$ is the Heaviside enriched degree of nodal freedom, $\mathbf{b}$ is the crack tip field function enriched degree of nodal freedom; in addition, the cell nodal forces vector $\mathbf{f} = \{\mathbf{f_u}, \mathbf{f_a}, \mathbf{f_b}, \mathbf{f}^{coh}\}$, in which the subscripts $\mathbf{u}$, $\mathbf{a}$ and $\mathbf{b}$ represent traditional, Heaviside-enriched, and exact near-tip asymptotic field functions with enriched degrees of

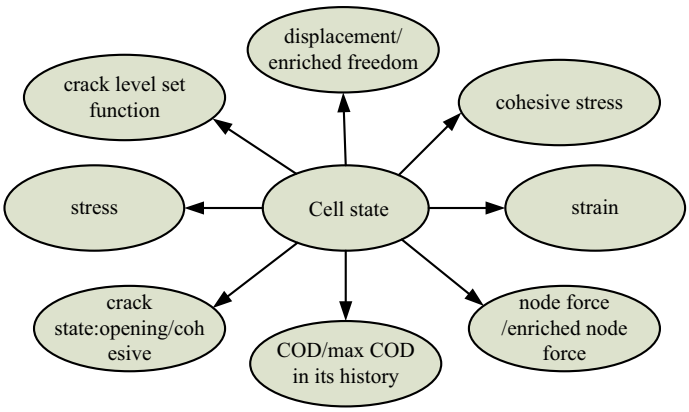

Fig. 5. Cell states.

nodal freedom, respectively, and c_s indicates the states of a cohesive cell. Based on the above cohesive cellular automata model, the states of a cohesive cell can be given as shown in Fig. 5.

3.3.2. Continuity to discontinuity model

In the CDCA and cohesive crack models, discontinuity may exist in some cellular elements, which include a crack opening element, cohesive crack element, and mixed element, which are shown in Fig. 6. The location of the crack, COD, and maximum COD on its history will determine the cellular node type, cellular element type, and cellular automaton model. In addition, with this method, the crack path is tracked based on the level set functions. By way of the level set values, the COD and maximum COD on its history, the node cellular type, the element cellular type, and the cellular automaton model are updated, particularly for certain cells, which change from a continuous cellular automaton model to a discontinuous cellular automaton model, from a cohesive crack element to a crack opening element, and so on.

3.3.3. Model updating

First, we define a cohesive crack vector $\mathbf{C} = \{c_s, \mathbf{w}_c, \mathbf{w}_c^m, \mathbf{f}^{coh}\}$, whose initial value is $C = \{0, \mathbf{0}, \mathbf{0}, \mathbf{0}\}$. Considering a cellular node N_i for a plane stress problem, the displacement of this node can be obtained owing to the effects of the nodal force vector $\mathbf{f}_i = \{\mathbf{f}_i^u, \mathbf{f}_i^a + \mathbf{f}_i^{coh}, \mathbf{f}_i^b + \mathbf{f}_i^{coh}\}$, opening crack element stiffness matrix $\mathbf{k}_i^u$, and stiffness related to cohesive $\mathbf{k}_i^c$, and can restrict all degrees of nodal freedom on its neighbor cell nodes N_i^k, which can be found in [45,47–49]. We can then obtain a new cohesive crack vector, and renew the stiffness matrix as $\mathbf{K} = \mathbf{k}_i^u + \mathbf{k}_i^{a,b} + \mathbf{k}_i^c$ when $c_s = 1$. The stiffness matrix then becomes $\mathbf{K} = \mathbf{k}_i^u$ when $c_s = 0$. According to the state of the crack surface and the cohesive crack model, the cohesive stress $\mathbf{f}^{coh}$ can be obtained. The relationship between the incremental force and incremental deformation can be reflected in two steps. First, the nodal force increment $\Delta\mathbf{f}_i = \{\Delta\mathbf{f}_i^u, \Delta\mathbf{f}_i^a + \Delta\mathbf{f}_i^{coh}, \Delta\mathbf{f}_i^b + \Delta\mathbf{f}_i^{coh}\}$ will lead cell node N_i to produce the displacement increment, $\Delta\mathbf{u}_i^h = \{\Delta\mathbf{u}_i, \Delta\mathbf{a}_i, \Delta\mathbf{b}_i\}$. The displacement increment $\Delta\mathbf{u}_i^h$ on cell node N_i will then lead its neighboring cell nodes to produce nodal force increment $\Delta\mathbf{f}_i^k$, and at the same time, $\Delta\mathbf{u}_i^h = \{\Delta\mathbf{u}_i, \Delta\mathbf{a}_i, \Delta\mathbf{b}_i\}$ will cause changes to the crack surface state c_s and cohesive crack vector $\mathbf{C} = \{c_s, \mathbf{w}_c, \mathbf{w}_c^m, \mathbf{f}^{coh}\}$.

Therefore, the increment of nodal force leads to the increment of nodal displacement, and the increment of nodal displacement leads to the increment of nodal force for its neighboring nodes, until static equilibrium of the system is achieved; in other words, a self-organization phenomenon of $\Delta\mathbf{u}_i^h \to 0$ and $\Delta\mathbf{f}_i^k \to 0$ appears. Thus, the updating steps for the cohesive crack problem can be given as follows:

(1) Obtain the updating order for all cells, and construct an adaptive updating scheme [58]. First, according to the nodal force matrix, one can obtain unbalanced nodal force F_{a_i}, and can further obtain the updating order set $\{\ a_1, a_2, \ldots, a_{n_t}\}$, in which the unbalanced nodal force should satisfy $F_{a_1} \geqslant F_{a_1+1}$.
(2) Initialize the cohesive crack state and stiffness matrix, and assume that the entire crack is opening, i.e., $c_s = 0$, $\mathbf{w}_c^m = \mathbf{w}_c = \mathbf{0}$ and $\mathbf{f}^{coh} = 0$.
(3) According to the cohesive crack vector $\mathbf{C} = \{c_s, \mathbf{w}_c, \mathbf{w}_c^m, \mathbf{f}^{coh}\}$, update the nodal stiffness matrix $\mathbf{K}_i$ and nodal force increment $\Delta\mathbf{f}_i$.
(4) Constrain all degrees of nodal freedom on all neighboring cells N_i^k, as shown in Fig. 7. According to the system function of the CA method, $\mathbf{K}_i\Delta\mathbf{u}_i^h = \Delta\mathbf{f}_i$, in which $\Delta\mathbf{f}_i = \{\Delta\mathbf{f}_i^u, \Delta\mathbf{f}_i^a + \Delta\mathbf{f}_i^{coh}, \Delta\mathbf{f}_i^b + \Delta\mathbf{f}_i^{coh}\}$. Calculate the increment of degrees of nodal freedom $\Delta\mathbf{u}_i^h$ using the increment of nodal force $\Delta\mathbf{f}_i$.

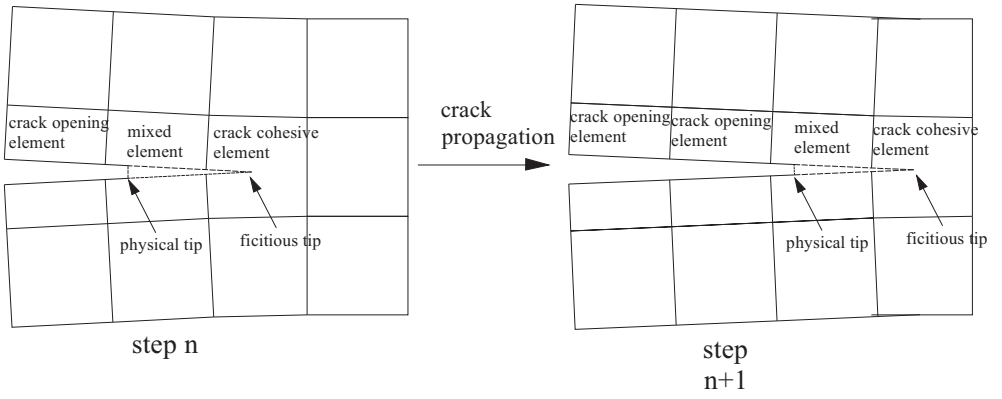

Fig. 6. Continuity to discontinuity model.

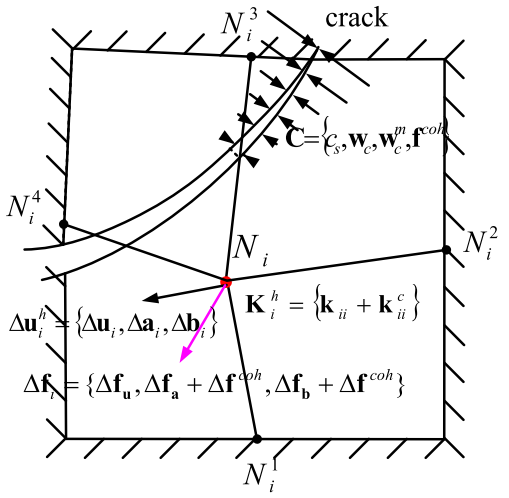

Fig. 7. Local updating model.

(5) Obtain the nodal force increment $\Delta\mathbf{f}_i^k$ of the neighboring cell N_i^k through $\Delta\mathbf{u}_i^h$ of cell N_i from the following equation: $\Delta\mathbf{f}_i^k=\mathbf{K}_i^k\Delta\mathbf{u}_i^h$.

(6) According to the results of steps (2) and (3), update the cohesive crack vector $\mathbf{C}=\{c_s,\mathbf{w}_c,\mathbf{w}_c^m,\mathbf{f}^{coh}\}$. Obtain crack opening displacement $\mathbf{w}_c$ and cohesive stress $\Delta\mathbf{f}_i^{coh}$.

(7) Apply steps (2) through (5) on all cellular nodes until $\Delta\mathbf{f}_i^k<\varepsilon_f$, $\Delta\mathbf{u}_i^h<\varepsilon_u$, and cohesive crack vector $\mathbf{C}=\{c_s,\mathbf{w}_c,\mathbf{w}_c^m,\mathbf{f}^{coh}\}$ no longer changes between the last two iterations.

Similar to other methods regarding the contact and cohesive problems, the convergence of the present method is influenced by the secant stiffness values k_n and k_s, and both a much larger and much smaller secant stiffness can lead to difficulty of convergence. After optimization through a numerical example, $10^{-1}E\leqslant k_n\leqslant 10^3E$ and $10^{-2}E\leqslant k_n\leqslant 10^2E$ can be easily converged, and the iteration number is determined based on the secant stiffness, crack state, and crack number; for example, with a 20,000 cell structure with one straight crack, only several hundred updating steps are needed for this method, and no more than one-hundred Newton iterations are needed for a cohesive iteration.

4. Adaptive near-tip improvement

4.1. Crack propagating path tracking

Based on the CA model, a new method was developed in this study to track the crack propagating path, which combines cell space cutting, cell neighbor searching, and the distance value to crack the surface and front. Differing from the level set method, the crack path tracking of the present method is only located on some of the local cells, which can considerably improve the calculation efficiency compared to a global search of the level set method.

First, assuming that one crack tip is located in cell C_1, according to the neighbor information and crack path location, the crack path will cut the line connecting nodes 1 and 2, and based on nodes 1 and 2 and the CA model, the next cutting cell C_2 can be easily obtained. According to this rule, until all cut cells for the whole crack path are obtained, which can be seen in Fig. 8. For all cut cells, the distance values ϕ_i and φ from each cell node to the crack surface and crack front are calculated, and then based on these two distance values, we can precisely track the cracks. Using the entire process of the present method, it can be seen that the calculation is located on the local cells, and the data saved are only the values for such cells.

First, a normal vector of crack surface $\mathbf{e}_2(\mathbf{x},t)$ is defined, which can be seen in Fig. 9, and the moving crack surface of interest can then be represented as a zero distance function of $\varphi_j(\mathbf{x},t)$. Through this method, the discontinuities are independent of the calculation grid. In general, a crack surface and some other discontinuities can be expressed as a distance function of $\varphi_j(\mathbf{x},t)=0$, and we can obtain the following:

$$\varphi_j(\mathbf{x},t)=\min_{\mathbf{x}_{\Gamma_j}\in\Gamma_j}\|\mathbf{x}-\mathbf{x}_{\Gamma_j}\|\frac{(\mathbf{x}-\mathbf{x}_{\Gamma_j})\cdot\mathbf{e}_2}{\|(\mathbf{x}-\mathbf{x}_{\Gamma_j})\cdot\mathbf{e}_2\|} \tag{26}$$

where Γ_j denotes the calculating crack, and $\mathbf{x}_{\Gamma_j}$ is the nearest point on crack Γ_j to source point $\mathbf{x}$.

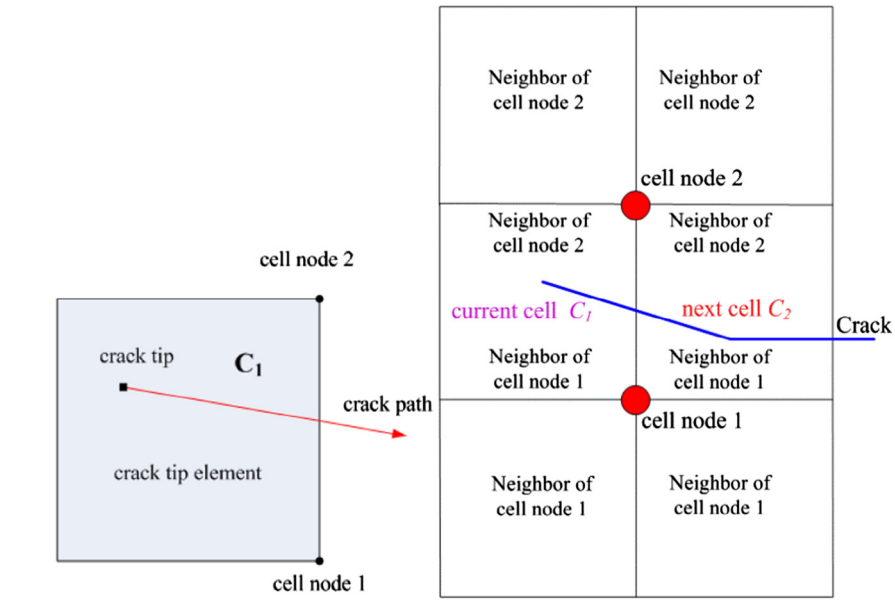

(a) Crack tip cell (b) Neighbor information and cell cutting

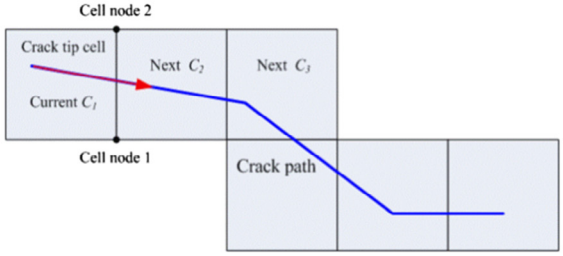

(c) Crack path and all cutting cells

Fig. 8. Crack tracking model.

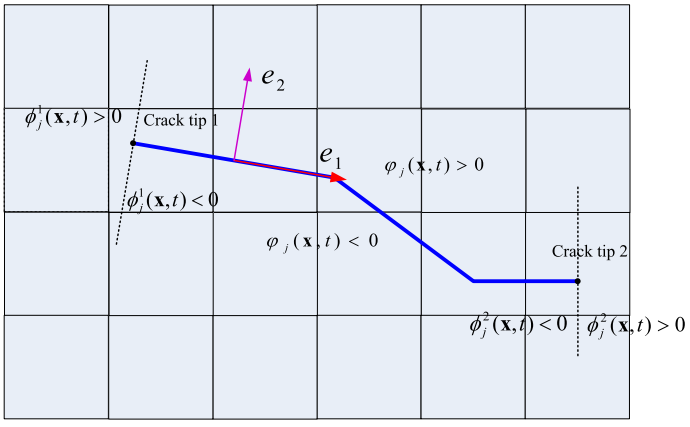

Fig. 9. Distance function of crack path tracking.

For a crack, only one distance function $\varphi_j(\mathbf{x},t)$ is generally insufficient to track the crack path, and similar to the crack surface function, a crack path in a positive direction is defined as $\mathbf{e}_1(\mathbf{x},t)$, and thus another distance function $\phi_j^i(\mathbf{x},t)$ at

the crack front is employed for this method. A growing crack front is tracked by representing the crack as the zero distance function $\phi_j^i(\mathbf{x},t)$. Two distance functions $\phi_j^1(\mathbf{x},t)$ and $\phi_j^2(\mathbf{x},t)$ for each crack front are then applied.

$$\begin{aligned}\phi_j^1(\mathbf{x},t) &= -\min_{\mathbf{x}_{\Gamma_j}\in\Gamma_j}\|(\mathbf{x}-\mathbf{x}_{\Gamma_j})\|\frac{(\mathbf{x}-\mathbf{x}_{\Gamma_j})\cdot e_1}{\|(\mathbf{x}-\mathbf{x}_{\Gamma_j})\cdot e_1\|}\\ \phi_j^2(\mathbf{x},t) &= \min_{\mathbf{x}_{\Gamma_j}\in\Gamma_j}\|(\mathbf{x}-\mathbf{x}_{\Gamma_j})\|\frac{(\mathbf{x}-\mathbf{x}_{\Gamma_j})\cdot e_1}{\|(\mathbf{x}-\mathbf{x}_{\Gamma_j})\cdot e_1\|}\end{aligned} \tag{27}$$

4.2. Adaptive improvement

As shown in Fig. 10, an unacceptable error can occur when the crack surface is not straight and a traditional unimproved local coordinate system is used. For example, with $\theta = -\sin^{-1}\left(\frac{d_b}{d_{OP}}\right) < 0$, in which d_{OP} is the distance between points O and P, and P is actually located within the domain of $\mathbf{n}_+$, $\theta > 0$ must be satisfied; however, under a traditional local coordinate system, $\theta < 0$ can be obtained, and the error is unacceptable. Thus, an adaptive near-tip improvement is proposed for the present method. To obtain a much more accurate angle of the enrichment functions, Belytschko and Black [59] proposed a scheme for obtaining the spatial derivatives of the enriching functions in the original global coordinate system, where a chain rule between the old and new coordinates is constructed. Differing from the method by Belytschko and Black, an adaptive improvement is developed through this method, in which the approximate angle for each field point is calculated exactly, which is much simpler and more efficient than the method proposed by Belytschko and Black.

As described in the previous section, the distance to the crack surface is employed for tracking the crack propagating path, and the distance $\varphi(\mathbf{x},t)$ to crack surface Γ for point P can then be given as $\varphi(\mathbf{x},t) = \min_{\mathbf{x}_\Gamma\in\Gamma_t}\|\mathbf{x}-\mathbf{x}_\Gamma\|\cdot\text{sign}(\mathbf{n}_+\cdot(\mathbf{x}-\mathbf{x}_\Gamma))$; in addition, the global coordinate of source point P is $\mathbf{x}$, $\mathbf{x}_\Gamma$ is any point on a crack surface that is nearest to point $\mathbf{x}$, and $\mathbf{n}_+$ is a unit normal vector to the crack surface. At this time, we define the local polar coordinate angle as

$$\theta = arctg\left(\frac{d}{d_{OA}}\right)\cdot sign(\varphi(\mathbf{x},t)) = arctg\left(\frac{\varphi(\mathbf{x},t)}{d_{OA}}\right)\varphi(\mathbf{x},t)\neq 0 \tag{28}$$

$$\theta = \pi\varphi(\mathbf{x},t) = 0,\ \mathbf{x}\in n+,\ \text{and} \tag{29}$$

$$\theta = -\pi\varphi(\mathbf{x},t) = 0,\ \mathbf{x}\in n- \tag{30}$$

where d_{OA} is the distance between crack tip O and nearest point A on the crack surface of point $\mathbf{x}$.

With this method, the sign of the local coordinate angle is always exact, and is always consistent with the location on the local crack surface.

4.3. Example of an adaptive improvement

An example for this adaptive improvement can be seen in Fig. 11, and we assume that $\theta > 0$ when A is located on top of the crack surface, and $\theta < 0$ when A is located below the crack surface. For this case, the exact polar angle is $\theta = \pi$. In addition, for a traditional local coordinate system, the polar angle of A is given as

$$\theta = (n_1-)\cdot arctg\left(\frac{d_1}{d_3}\right) < 0 \tag{31}$$

and the error of this coordinate system is then $e = \|\pi-\theta\| > \pi$, and the relative error is greater than 100%. In addition, for the present improved coordinate system, the polar angle of A can be obtained using

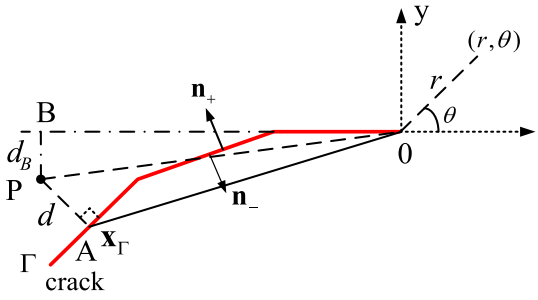

Fig. 10. Local coordinate system for a crack tip.

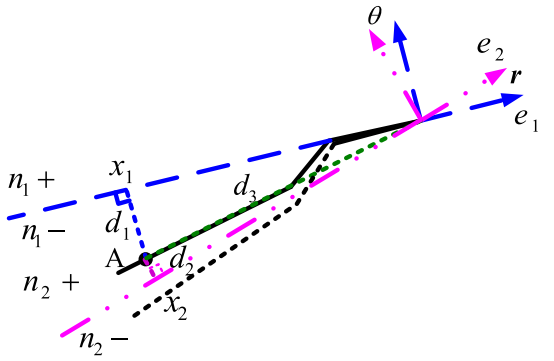

Fig. 11. Example of a local coordinate system.

$$\theta = (n_2+)\cdot arctg\left(\frac{d_2}{d_3}\right) \approx \pi \tag{32}$$

It can be seen in Eq. (28) that $d_2 \gg d_3$, and the polar angle for the improvement coordinate system is then close to the exact value π, and thus the present adaptive improvement is efficient.

5. Numerical examples

To certify the efficiency of the present continuous-discontinuous cellular automaton method for cohesive crack propagation modeling, the failure processes of two rock specimens are considered, which are given as follows.

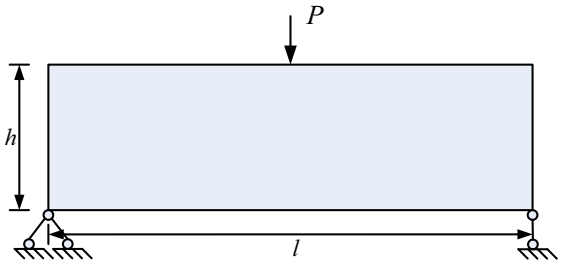

Fig. 12. Model of three-point bending rock beam.

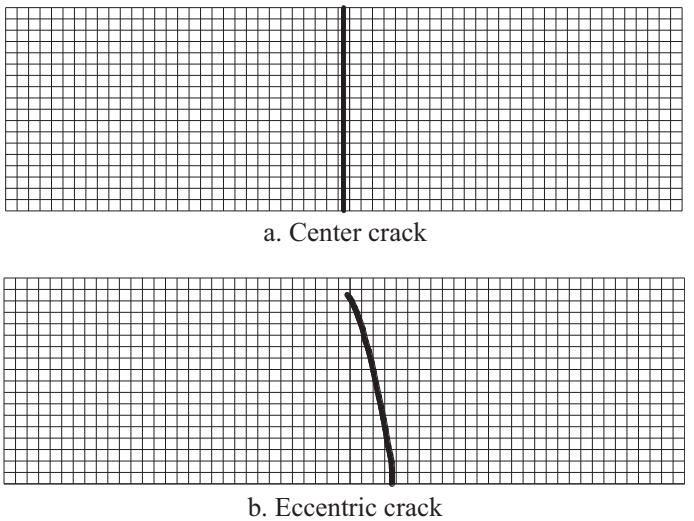

Fig. 13. Crack propagation paths for three-point bending specimen.

5.1. Three-point bending rock specimen

A simply supported rock beam is considered in this section, in which an imposed displacement is loaded on the top edge at the center of the beam, as shown in Fig. 12. The physical and mechanical properties of the material are as follows: Young's modulus $E = 100$ MPa, Poisson's ratio $v = 0.0$, tensile strength $f_t = 1.0$ MPa, and fracture energy $G_f = 0.1\ \frac{\mathrm{N}}{\mathrm{mm}}$. The geometry of the model is as follows: the length of the specimen is $l = 10$ mm, the height of the specimen is $h = 3$ mm, and the depth is $d = 1$ mm. In addition, 1062 elements are used for the entire calculation in this three-point bending specimen.

Fig. 13 shows the crack propagation paths for the three-point bending specimen for two different initial crack locations, where the initial crack shown in Fig. 13(a) is located at the center of the beam, and the initial crack shown in Fig. 13(b) is located 0.7 mm from the center of the beam. It can be seen in Fig. 13(a) that the center crack propagates directly upward

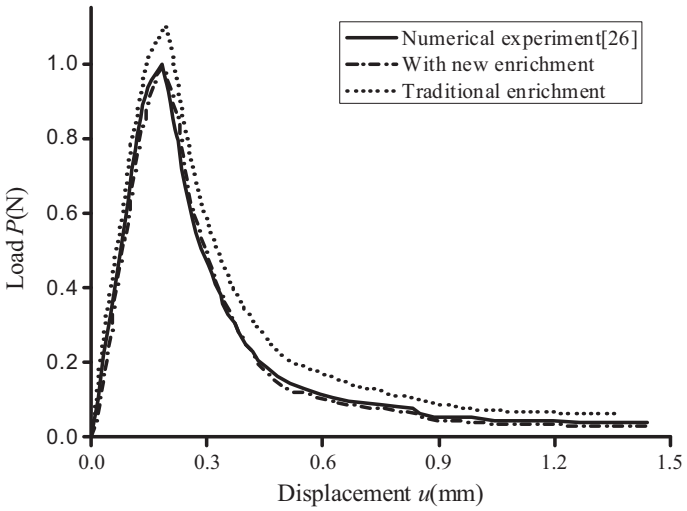

Fig. 14. Load-displacement response with different method.

Table 1
Original propagating angle for different methods.

Method	Initial propagating angle	
	Traditional enrichment	Enrichment of Eq. (12)
Center crack	0.01041	0.00015
Eccentric crack	0.25841	0.25243

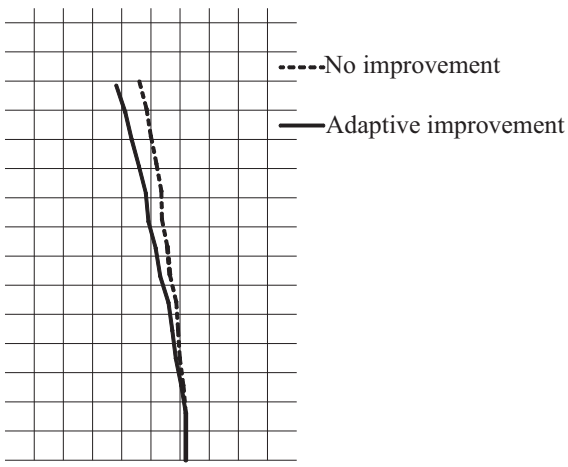

Fig. 15. Comparison for growth path with and without adaptive improvement.

toward the load point, and Fig. 13(b) shows that an eccentric crack also propagates offset from the initial line and toward the load point, which shows agreement with the results from the method in [26].

The load displacement response of a three-point bending specimen with a center crack is shown in Fig. 14, in which a comparison is given between with and without new enrichment and numerical experimental results by Wells and Sluys [26]. one can see that the present method results with new enrichment agree well with the results by the numerical experiments in [26], and loads are much larger than that without the new enrichment at the same displacements, then the response with new enrichment is much more close to the numerical experimental results by Wells and Sluys [26].

To compare the efficiency of the present enrichment function, the initial propagating angles by different enrichment functions are described in this section, which can be seen in Table 1, and the initial propagating angles in this table are obtained using the present method, and only different enrichment functions are employed. One can see in this table that the present method can obtain a much more accurate angle for the center crack example; in addition, if the present enrichment functions are not singular at the crack tip, the integral accuracy may be much higher.

It can be seen in Fig. 15 that a comparison for growth path with and without adaptive improvement is plotted, in which one can see that the growth angle without improvement is much more smaller than that of numerical experiment results, and the reason is that without this improvement the errors of polar angle for some point is greater than 100%. With this improvement, the polar angle for curve crack is much more accurate.

Based on these results, one can see that the calculating grids are independent of the cracks, and the agreement in the results indicates the efficiency of the present method.

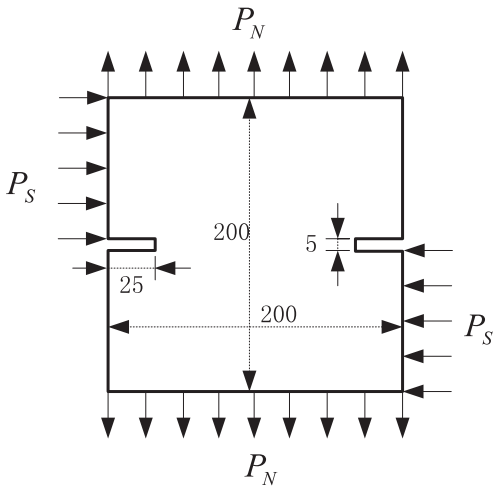

Fig. 16. Geometry and loading model of mixed mode fracture specimen.

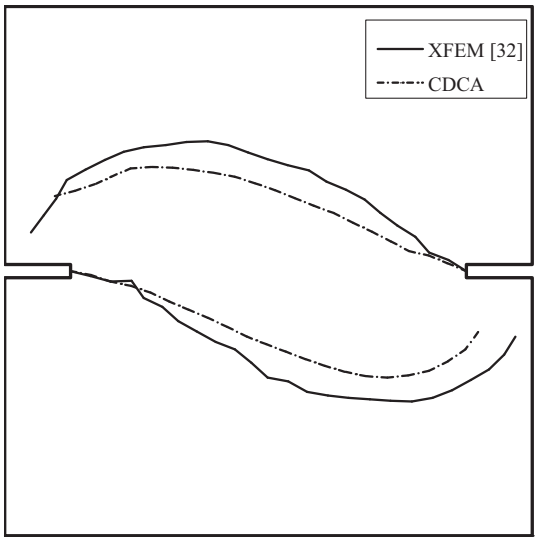

Fig. 17. Propagation paths with $P_S = 10$ kN for CDCA and XFEM.

5.2. Mixed mode fracture test for a rock specimen

A mixed mode fracture test, which was performed in [32], is described in this section. As can be seen in Fig. 16, the dimensions are 200 mm × 200 mm with a notch depth of 25 mm and width of 5 mm. The compressive and tensile strengths are given as $f_c = 46.24\ \frac{N}{mm^2}$ and $f_s = 3.67\ \frac{N}{mm^2}$, respectively. The Young's modulus is $E = 30\ \frac{kN}{mm^2}$, the Poisson ratio is $v = 0.2$, and the fracture energy is $G_f = 0.11\ \frac{N}{mm}$. In addition, a shear load P_S and normal load P_N are considered.

Similar to [32], a shear load force P_S is subsequently kept constant, and the specimens are loaded in the normal direction by loading P_N. The maximum circumferential stress is employed in this section, and 10,000 elements are considered for this example.

The crack propagating paths obtained for a shear load of $P_S = 10$ kN are given in Fig. 17, and it can be seen that the results of the present method are very close to those using XFEM [32]. Fig. 18 plots the load displacement response for a shear load of $P_S = 10$ kN, and it can be seen that the curve of the load and displacement is very close between the present method and XFEM [32], and that the peak loads in the normal direction obtained from both methods are much higher than that from the experiment.

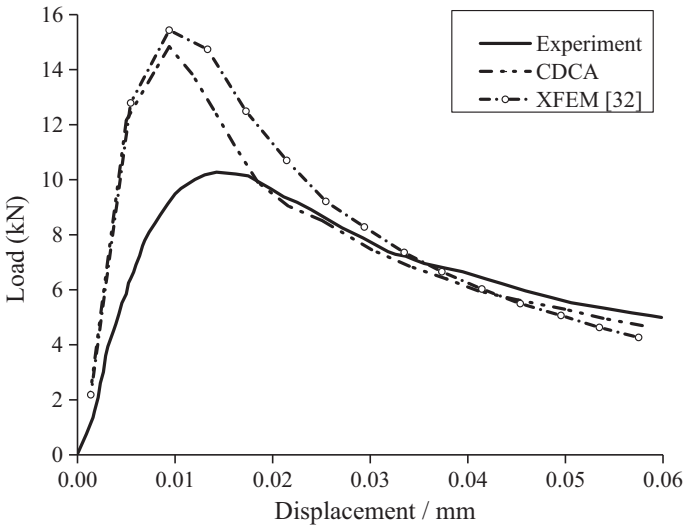

Fig. 18. Load-displacement response for mixed mode fracture test with $P_S = 10$ kN.

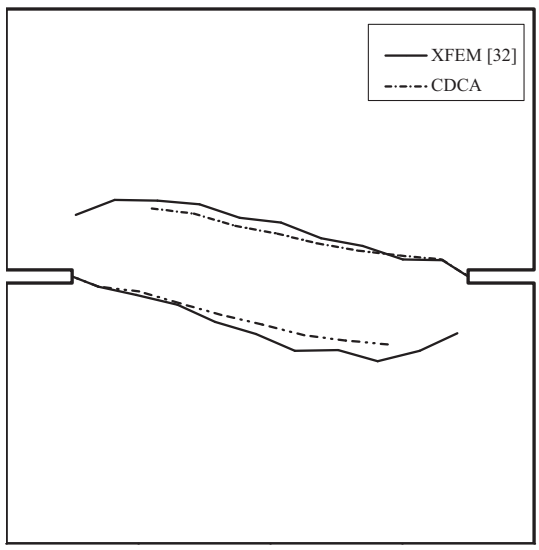

Fig. 19. Propagation paths with $P_S = 5$ kN for CDCA and XFEM.

Similar results were obtained for a shear load of $P_S = 5$ kN, as illustrated in Fig. 19, where it can also be seen that the propagation paths of the present method are very close to those achieved using XFEM [32]. In addition, Fig. 20 shows the load displacement response for a shear load of $P_S = 5$ kN, in which it can be seen that the curve from the present method agrees well with the curve achieved through the experiment, and that the peak load by XFEM [32] is much larger than that from the experiment [32].

The calculation of the present method is located in a local cell, and no assembled global stiffness matrix is needed during the entire calculation process, thereby saving a significant amount of computer memory, which can be seen in Fig. 21, in which the amount of computer memory required for XFEM is cut in half for the present method.

To compare the calculation efficiency between CDCA and XFEM, the CPU times for different cell numbers are plotted in Fig. 22. It can be seen that the computer time required by the present method is a little long than that of XFEM, which will be overcome by the fast successive over-relaxation updating method used in a follow-up work on CDCA, which will greatly improve its calculation efficiency. The computer system used for the calculation is as follows: Intel Core 2 Duo E8400 CPU @ 3.0 GHz, 4 GB of memory, and Windows 7 operating system.

Fig. 23 shows the convergence of the present method, in which the average error for some fixed nodes indicates the relative error of displacement between the present method and the experiment, and the load is from 4 to 12 kN, error $= |d_N - d_E|$, where d_N denotes the vertical displacement of the present method on the center point of the upper sides

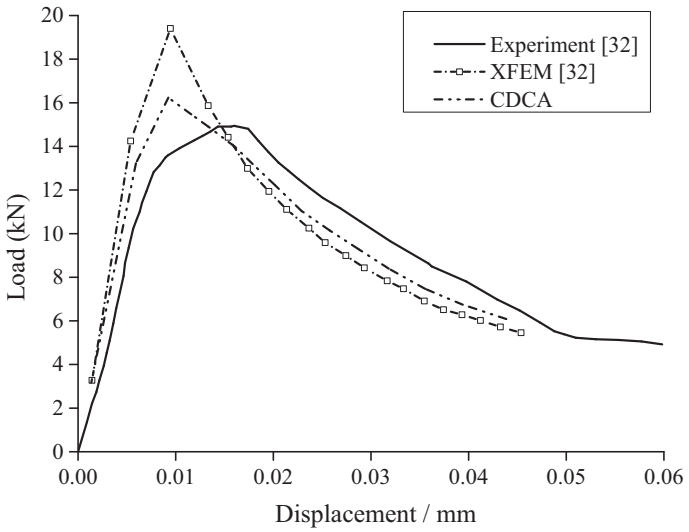

Fig. 20. Load-displacement response for mixed mode fracture test with $P_S = 5$ kN.

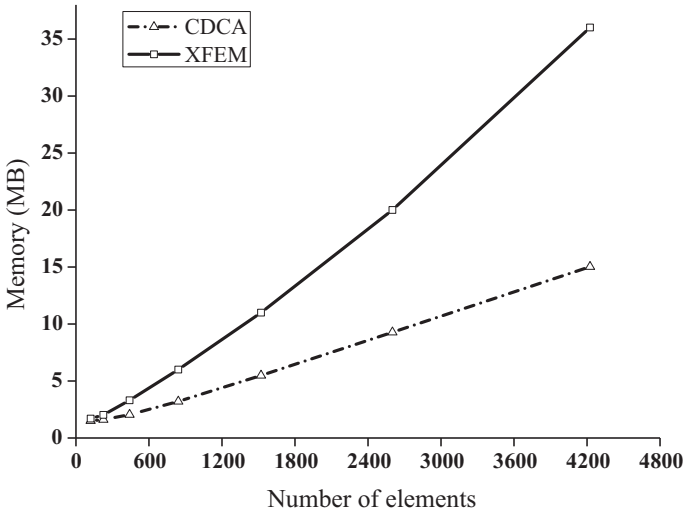

Fig. 21. Comparison of computer memory use between CDCA and XFEM.

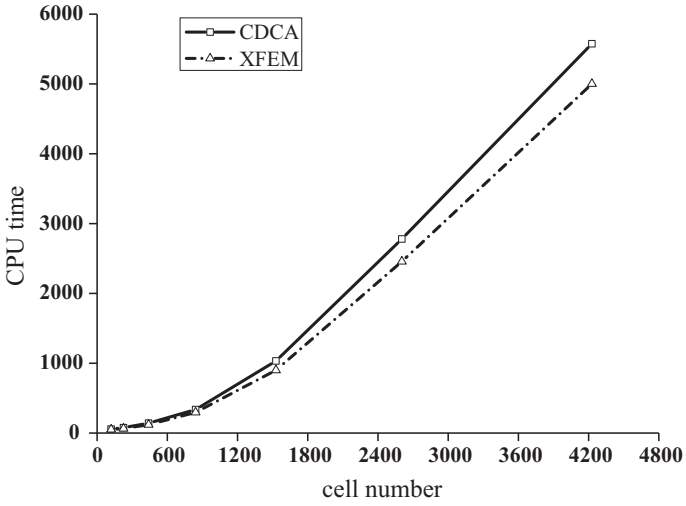

Fig. 22. Comparison of CPU time between CDCA and XFEM.

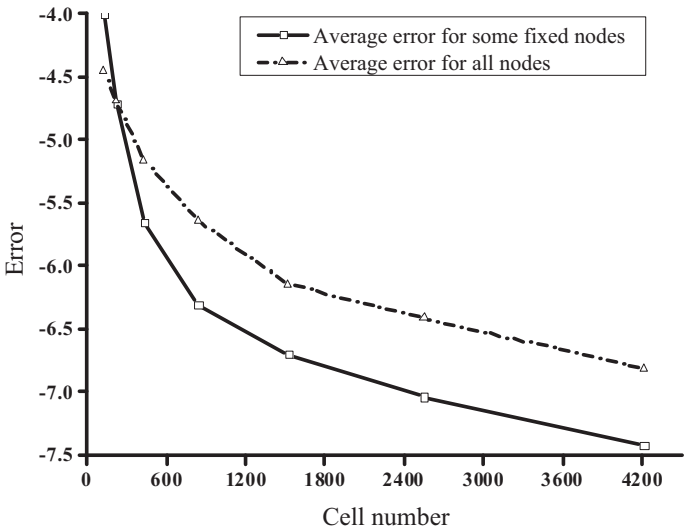

Fig. 23. Convergence of the present method.

of square, and d_E denotes the vertical displacement through the experiment on the center point of the upper sides of square. And the average error for some all nodes indicates the relative error of displacement between the present method and the numerical results with 96,000 elements on all corresponding nodes. Here, it can be seen that the average relative error decreases with the increase in the number of cells.

6. Conclusion

In the present paper, the implantation of a continuous-discontinuous cellular automaton (CDCA) method for cohesive crack propagation modeling was described in detail. With a cohesive crack model, no singularities occur at the crack tip, and therefore, the crack tip enrichment with singular functions is not suitable; thus, a group of new nonsingular additional enrichment functions are employed instead of the traditional singular enrichment functions, which are consistent with the nonsingular asymptotic stress field around a cohesive crack tip. Aiming at a devious crack path, improvement in the adaptive crack tip polar coordinate is proposed for treating the local polar coordinate error caused by a devious crack-fracturing segment. Based on the cohesive crack model for quasi-brittle materials, a cellular automation model for a cohesive crack was developed, including a cell model, cell state, and updating rules. Combining the above theories, CDCA for a cohesive crack analysis was proposed, through which the cracking path can pass through any element, and no re-meshing is needed. In

addition, the calculation is only limited to the cell locality, and no assembled global stiffness is required, which can avoid certain difficulties caused by the different nodal freedoms for different nodes. Finally, some examples were given to show that the proposed approach is efficient and accurate for simulations of cohesive crack growth in concrete and rock and can be widely applied to certain areas of practical rock engineering.

Acknowledgments

The work was financially supported by the National Natural Science Foundation of China (No. 11232014, 51621006), the International Partnership Program of the Chinese Academy of Sciences (115242KYSB20160017), and the Youth Innovation Promotion Association CAS (No. 2014304).

References

[1] Barenblatt GI. The formation of equilibrium cracks during brittle fracture: general ideas and hypotheses, axially symmetric cracks. J Appl Math Mech 1959;23:622–36.
[2] Dugdale DS. Yielding of steel sheets containings slits. J Mech Phys Solids 1960;8:100–4.
[3] Dei PS, Iori I. Osservazioni e rilievi sul comportamento a trazione dei calcestruzzi: analisi di risultanze sperimentali. Studi e Ricerche 1986;8:35–62.
[4] Ngo D, Scordelis AC. Finite element analysis of reinforced concrete beams. J Am Concr Inst 1967;64:152–63.
[5] Hillerborg A, Modeer M, Petersson PE. Analysis of crack formation and crack growth by means of fracture mechanics and finite elements. Cem Concr Res 1976;1:773–82.
[6] Elices M, Guinea GV, Gomez J, Planas J. The cohesive zone model: advantages, limitations and challenges. Eng Fract Mech 2002;69:137–63.
[7] Carpinteri A. Post-peak and post-bifurcation analysis of cohesive crack propagation. Eng Fract Mech 1989;32:265–78.
[8] Moes N, Dolbow J, Belytschko T. A finite element method for crack growth without remeshing. Int J Numer Meth Eng 1999;46:131–50.
[9] Li S, Ghosh S. Extended Voronoi cell finite element model for multiple cohesive crack propagation in brittle materials. Int J Numer Meth Eng 2006;65:1028–67.
[10] Zamani A, Eslami MR. Embedded interfaces by polytope FEM. Int J Numer Meth Eng 2011;88:715–48.
[11] Bolzon G, Cocchetti G. Direct assessment of structural resistance against pressurized fracture. Int J Numer Anal Meth Geomech 2003;27:353–78.
[12] Bolzon G, Corigliano A. Finite elements with embedded displacement discontinuity: a generalized variable formulation. Int J Numer Meth Eng 2000;49:1227–66.
[13] Yang ZJ, Deeks AJ. Modelling cohesive crack growth using a two-step finite element-scaled boundary finite element coupled method. Int J Fract 2007;143:333–54.
[14] Ooi ET, Song C, Loi FT, Yang ZJ. Automatic modeling of cohesive crack propagation in concrete using polygon scaled boundary finite elements. Eng Fract Mech 2012;93:13–33.
[15] Oliveira HL, Leonel ED. Cohesive crack growth modelling based on an alternative nonlinear BEM formulation. Eng Fract Mech 2013;111:86–97.
[16] Saleh AL, Aliabadi MH. Crack-growth analysis in concrete using boundary element method. Eng Fract Mech 1995;51:533–45.
[17] Yang B, Ravi-Chandar K. A single-domain dual boundary element formulation incorporating a cohesive zone model for elastostatic cracks. Int J Fract 1998;93:115–44.
[18] Cen Z, Maier G. Bifurications and instabilities in fracture of cohesive-softening structures: a boundary element analysis. Fatigue Fract Eng Mater Struct 1992;15:911–28.
[19] Maier G, Novati G, Cen Z. Symmetric galerkin boundary element method for quasi-brittle-fracture and frictional contact problems. Comput Mech 1993;13:74–89.
[20] Chen T, Wang B, Cen Z, Wu Z. A symmetric galerkin multi-zone boundary element method for cohesive crack growth. Eng Fract Mech 1999;63:591–609.
[21] Belytschko T, Lu Y, Gu L. Element-free Galerkin methods. Int J Numer Meth Eng 1994;37:229–56.
[22] Rabczuk T, Zi G. A meshfree method based on the local partition of unity for cohesive cracks. Comput Mech 2007;39:743–60.
[23] Rabczuk T, Zi G, Bordas S, Nguyen-Xuan H. A geometrically non-linear three-dimensional cohesive crack method for reinforced concrete structures. Eng Fract Mech 2008;75:4740–58.
[24] Goudarzi M, Mohannadi S. Analysis of cohesive cracking in saturated porous media using an extrinsically enriched EFG method. Comput Geotech 2015;63:183–98.
[25] Jaskowiec J, Cichon C. Coupling of FEM and EFGM with dynamic decomposition in 2D quasi-brittle crack growth analysis. Comput Assist Meth Eng Sci 2004;11:293–320.
[26] Wells GN, Sluys LJ. A new method for modeling cohesive cracks using finite elements. Int J Numer Meth Eng 2001;50:2667–82.
[27] Moes N, Belytschko T. Extended finite element for cohesive crack growth. Eng Fract Mech 2002;69:813–33.
[28] Zi G, Belytschko T. New crack-tip elements for XFEM and applications to cohesive cracks. Int J Numer Meth Eng 2003;57:2221–40.
[29] Mariani S, Perego U. Extended finite element method for quasi-brittle fracture. Int J Numer Meth Eng 2003;58:103–26.
[30] Mergheim J, Kuh E, Steinmann P. A finite element method for the computational modelling of cohesive cracks. Int J Numer Meth Eng 2005;63:276–89.
[31] Cox JV. An extended finite element method with analytical enrichment for cohesive crack modelling. Int J Numer Meth Eng 2009;78:48–83.
[32] Unger JF, Eckardt S, Konke C. Modeling of cohesive crack growth in concrete structures with the extended finite element method. Comput Methods Appl Mech Eng 2007;196:4087–100.
[33] Ahmed A, Sluys LJ. Anomalous behavior of bilinear quadrilateral finite elements for modeling cohesive cracks with XFEM/GFEM. Int J Numer Meth Eng 2013;94:454–72.
[34] Jaskowiec J, Meer FP. A consistent iterative scheme for 2D and 3D cohesive crack analysis in XFEM. Comput Struct 2014;136:98–107.
[35] Ortiz M, Leroy Y, Needleman A. A finite element method for localized failure analysis. Comput Methods Appl Mech Eng 1987;61:189–214.
[36] Jirasek M. Comparative study on finite element with embedded discontinuities. Comput Methods Appl Mech Eng 2000;188:307–30.
[37] Eugenio A, Rasetti M. A cellular automaton for elasticity equations. Int J Mod Phys B 1996;10:203–18.
[38] Olami Z, Feder HJS, Christensen K. Self-organized criticality in a continuous, nonconservative cellular automaton modeling earthquakes. Phys Rev Lett 1992;68:1244–8.
[39] Abdellaoui M, EI Jai A, Shillor M. Cellular automata model for a contact problem. Math Comput Model 2002;36:1099–114.
[40] Canyurt OE, Hajela P. A cellular framework for structural analysis and optimization. Comput Methods Appl Mech Eng 2005;194:3516–34.
[41] Shen C, Dai S, Yang J, Tang X. Cellular automata for analysis of plane problem in theory of elasticity. J f Tsinghua Univ (Sci & Tech) 2001;41:35–8.
[42] Gurdal Z, Tatting T. Cellular automata for design of truss structures with linear and non-linear response. In: Proceedings of 41st AIAA/ASME/ASCE/AHS/ASC structural dynamics and materials conference, Atlanta, GA; 2000.
[43] Hopman RK, Leamy MJ. Triangular cellular automata for computing two-dimensional elastodynamic response on arbitrary domain. J Appl Mech – ASME 2011;78:021020.
[44] Leamy MJ. Application of cellular automata modeling to seismic elastodynamics. Int J Solids Struct 2008;45:4835–49.

[45] Feng XT, Pan PZ, Zhou H. Simulation of the crack microfracturing process under uniaxial compression using an elasto-plastic cellular automaton. Int J Rock Mech Min Sci 2006;43:1091–108.
[46] Yan F, Feng XT, Pan PZ, Li SJ. A continuous-discontinuous cellular automaton method for cracks growth and coalescence in brittle material. Acta Mech Sinica 2014;30:73–83.
[47] Yan F, Feng XT, Pan PZ. Simulation of rock crack propagation using continuous-discontinuous cellular automaton method. In: Rock characterisation, modelling and engineering design methods – proceedings of the 3rd ISRM SINOROCK 2013 Symposium. Leiden: Taylor & Francis – Balkema; 2013. p. 403–8.
[48] Yan F, Feng XT, Pan PZ, Li SJ. Discontinuous cellular automaton method for crack growth analysis without remeshing. Appl Math Model 2014;38:291–307.
[49] Yan F, Feng XT, Pan PZ, Li YP. A continuous-discontinuous cellular automaton method for regular frictional contact problems. Arch Appl Mech 2013;83:1239–55.
[50] Popov VL, Psakhie SG. Theoretical principles of modeling elastoplastic media by movable cellular automata method. I. Homogenous media. Phys Mesomech 2001;4:15–25.
[51] Xiao S. A lattice Boltzmann method for shock propagation in solids. Commun Numer Methods Eng 2007;23:71–84.
[52] Kwon YW, Hosiglu S. Application of lattice Boltzmann method, finite element method and cellular automata and their coupling to wave propagation problems. Comput Struct 2008;86:663–70.
[53] Khvastunkov MS, Leggoe JW. Adapting cellular automata to model failure in spatially heterogenous ductile alloys. Scripta Mater 2004;51:309–14.
[54] Needleman A. An analysis of decohesion along an imperfect interface. Int J Fract 1990;42:21–42.
[55] Tvergaard V. Effect of fibre debonding in a whisker-reinforced metal. Mater Sci Eng, A 1990;125:203–13.
[56] Ortiz M, Pandolfi A. Finite-deformation irreversible cohesive element for three-dimensional crack-propagation analysis. Int J Numer Meth Eng 1999;44:1267–82.
[57] Xiao QZ, Karihaloo BL. Asympotic fields at frictionless and frictional cohesive crack tips in quasibrittle materials. J Mech Mater Struct 2006;1:881–910.
[58] Yan F, Feng XT, Lv JH, Pan PZ, Li SJ. An adaptive cellular updating scheme for the continuous-discontinuous cellular automaton method. Appl Math Model 2017;46:1–15.
[59] Belytschko T, Black T. Elastic crack growth in finite elements with minimal remeshing. Int J Numer Meth Eng 1999;45:601–20.